XAFS Studies of Nickel and Sulfur Speciation in Residual Oil Fly-Ash Particulate Matters (ROFA PM)

S I D H A R T H A   P A T T A N A I K , * , † , ‡
F R A N K   E .   H U G G I N S , ‡
G E R A L D   P .   H U F F M A N , ‡
W I L L I A M   P .   L I N A K , § A N D
C .   A N D R E W   M I L L E R §

Central Electrochemical Research Institute, Karaikudi − 630 006, Tamilnadu, INDIA, CFFS/CME, University of Kentucky, 533 S. Limestone St., Lexington, Kentucky 40506-0043, and NRMRI, Environmental Protection Agency, Research Triangle Park, North Carolina-27711

XAFS spectroscopy has been employed to evaluate the effect of fuel compositions and combustion conditions on the amount, form, and distribution of sulfur and nickel in size-fractionated ROFA PM. Analysis of S K-edge XANES establish that sulfate is abundant in all PM. However, depending upon the combustion conditions, lesser amounts of thiophenic sulfur, metal sulfide, and elemental sulfur may also be observed. Least-squares fitting of Ni K-edge XANES reveals that most of the nickel in PM is present as bioavailable $NiSO_4 \cdot nH_2O$. The insoluble Ni mainly exists as a minor species, as nickel ferrite in $PM_{2.5}$ (PM < 2.5 μm) and nickel sulfide, Ni_xS_y in $PM_{2.5+}$ (PM > 2.5 μm). The Ni K-edge XANES results are in agreement with the EXAFS data. Such detailed speciation of Ni and S in PM is needed for determining their mobility, bioavailability, and reactivity, and hence, their role in PM toxicity. This information is also important for understanding the mechanism of PM formation, developing effective remediation measures, and providing criteria for identification of potential emission sources. Transition metals complexing with sulfur is ubiquitous in nature. Therefore, this information on metal sulfur complex can be critical to a large body of environmental literature.

Introduction

Fossil fuel combustion is believed to be a major primary source of fine particulate matter (PM) in the ambient air. Extensive epidemiological studies suggest that elevated fine PM concentrations in the air are associated with morbidity and mortality from cardiovascular and respiratory illnesses (*1*). Annually, exposure to PM is estimated to cause approximately 500 000 premature deaths worldwide (*2*). Motivated by these statistics, the U.S. Environmental Protection Agency (EPA) promulgated new regulations governing the permissible level of air-borne PM less than 2.5 μm in diameter (*3*, *4*). Since then, numerous studies on the effect of PM on human health have focused attention on source $PM_{2.5}$, particularly those emitted from combustion of residual

oils rich in sulfur and transition metals. While these studies show $PM_{2.5}$ to be more closely associated with adverse health effects than $PM_{2.5+}$, it is not clear as to what specific compounds in the former pose the greatest health hazards (*3*).

In general, particulates are complex, comprising of elemental carbon, organic carbon compounds, and reactive components such as transition metals, metal oxides, sulfates, and nitrates. Given this complexity, systematic identification of toxicity due to a specific individual component is a challenging task. Although efforts to identify the root causes of adverse effects of PM have intensified in recent years, a definite answer has not yet been established (*4*). Recent EPA testing on laboratory animals exposed to fine PM from residual oil combustion suggests that a key factor contributing to adverse health impacts is the amount of water-soluble transition metals present in the PM (*5*, *6*). In parallel, some investigators studying the direct effects of PM on cells in culture have suggested that PM-generated oxidants and toxicity can be prevented by removing metals by chelating agents (*7*−*9*). Taken together these studies are quite consistent with the view that PM exposure leads to the delivery of metals to multiple extra-pulmonary sites, wherein they form reactive centers that continually catalyze the generation of reactive oxygen species (ROS) and induce severe oxidative stress (*10*).

While metals within PM in general may be toxic, the role of a specific metal is far from being fully understood. Several metals have been tested for their role in PM toxicity. Although universally high toxicity has been attributed to vanadium (*10*), nickel is generally not far behind (*11*). Nickel is a primary contributor to the inhalation cancer risk because of its relative high concentration in ROFA PM and the known carcinogenic potency of its sub-sulfide forms (Ni_3S_2) (*5*, *6*). For cardiovascular exposures in particular, Ni has been linked to the cardio-depressant effects of ROFA exposure (*12*, *13*). Nickel along with iron, vanadium, copper, and zinc have been shown to play a prominent role in inducing toxicity, triggering aggressive inflammatory responses in cultured lung cells, laboratory animals, and humans (*14*). Toxicological and occupational studies support the contention that particulate related illnesses are attributable to physicochemical characteristics of PM (*15*), and they emphasize the need for the development of novel analytical tools for detailed speciation of toxic components in PM. Traditionally, the chemical speciation of metals in environmental samples is either elucidated using chemical models based on equilibrium reactions or determined using wet-chemical methods relying on sequential extraction of various phases. However, these two approaches present serious limitations and are prone to artifacts (*16*). Conventional XRD technique, though nondestructive, is not sensitive to dilute or well dispersed metal species in PM.

Synchrotron-based XAFS spectroscopy has, in recent years, emerged as an important tool for trace metal speciation in PM (*17*). Being nondestructive, it preserves the chemical integrity of the sample and thus eliminates the need for sequential extraction method where sample loss and undesirable chemical reaction are of concern. In addition, the two modifications of XAFS [i.e., XANES and EXAFS] measure the X-ray absorption coefficients in different energy regions relative to the absorption edge of a target element, and render complementary information about the chemical nature of the PM. A preliminary account of Ni K-edge XAFS of ROFA PM has been presented earlier (*18*). Here we report the molecular structure and a detailed chemical speciation of S

* Corresponding author phone: 91-04565-224062; fax 91-04565-227779; e-mail: sidpattanaik@yahoo.com.
† Central Electrochemical Research Institute.
‡ University of Kentucky.
§ Environmental Protection Agency.

TABLE 1. Combustion Systems, Residual Oils, and Metals and Carbon Concentrations in PM Produced from Residual Oil Combustion

combustor	oil type, its S and ash contents (wt %)			fine PM/PM$_{2.5}$	metal (ppm) and C (wt %) concentrations			coarse PM / PM$_{2.5+}$	metal (ppm) and C (wt %) concentrations		
	type	S	ash		Fe	Ni	C		Fe	Ni	C
FTB	HS6[a]	2.33	0.10	HS6F	3850	8020	87	HS6C	2300	2270	96
	MS6	0.93	0.03	MS6F	4460	7470	79	MS6C	1510	1230	98
	LS6	0.53	0.02	LS6F	5100	4840	66	LS6C	1410	863	90
	BL5[b]	1.73	0.07	BL5F	4220	10600	64	BL5C	1110	2200	88
RLC	HS6	2.33	0.10	BL6F	13993	16518	0	n/a[c]			

[a] Derived from no. 6 oil. [b] Derived from no. 5 oil. [c] n/a, not applicable.
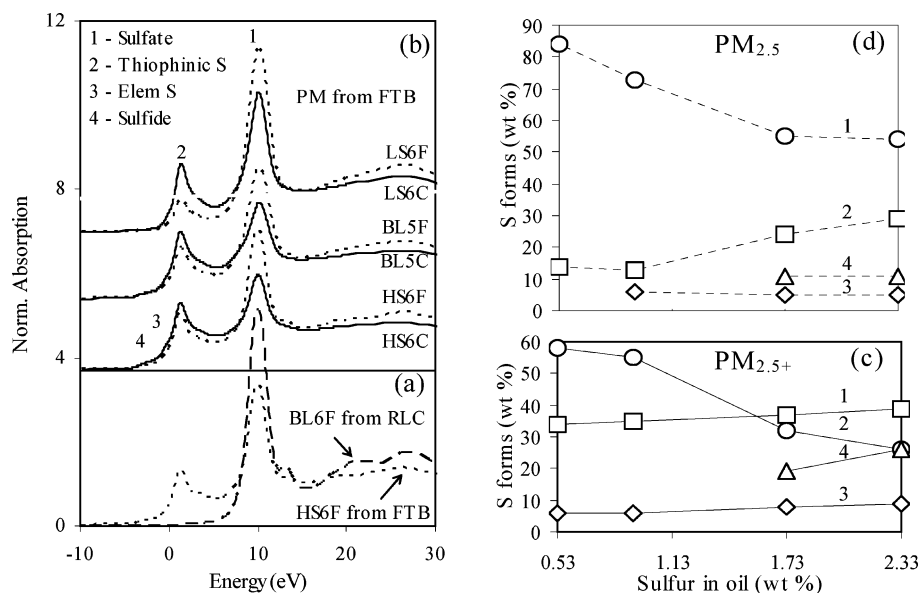

FIGURE 1. S K-edge XANES spectra of (a) two PM$_{2.5}$ samples obtained from same oil (HS6) burned in different combustors (FTB and RLC), (b) both PM fractions obtained from different oils burned in same combustor (FTB), and percentages of the total S contained by each identified S-form in (c) PM$_{2.5+}$, and (d) PM$_{2.5}$ as a function of S content (wt. %) in the oils.

and Ni in ROFA PM by combining XAFS spectroscopy with an aqueous leaching procedure.

Materials and Methods

Sample Generation. The residual oil combustion experiments were performed using a 732 kW three-pass fire tube boiler (FTB) and a 82 kW laboratory scale refractory-lined combustor (RLC). These two systems represent extremes of the range of practical conditions under which residual oils are burned. Three no. 6 residual oils (namely, low sulfur no. 6 (LS6), medium sulfur no. 6 (MS6), high sulfur no. 6 (HS6)) and one no. 5 residual oil, designated baseline no. 5 (BL5) were combusted (Table 1). ROFA PM were prepared from all four oils in the FTB under high gas quenching rate and short residence time resulting in PM rich in unburned char (~60–90% carbon). These PM exhibited a bimodal particle size distribution with a small accumulation mode and mean diameter 0.07–0.08 μm (*19*). A cyclone apparatus was used to separate them into fractions with mean diameter <2.5 μm (*fine* PM or PM$_{2.5}$) and >2.5 μm (*coarse* PM or PM$_{2.5+}$). Fine PM are designated LS6F, MS6F, BL5F, and HS6F, while coarse PM are designated LS6C, MS6C, BL5C, and HS6C in the remainder of the text (Table 1).

For comparison purposes, one PM$_{2.5}$, designated BL6F, was prepared in the RLC burning HS6 oil under a higher operating temperature with lower quenching rates and longer residence time. The particle emissions from this system contained essentially no unburned carbon and were more characteristic of the emissions from large oil-fired utility

boilers. The PM samples were collected on large Teflon-coated glass fiber filters, transformed to sampling jars and made available for XAFS and toxicological studies. The details of combustion experiments, sampling procedures, and the elemental compositions of the ROFA PM have been reported earlier (*19, 20*). Only the elemental compositions pertinent to this study are summarized in Table 1.

X-ray Absorption Measurements. The Ni and S K-edges fluorescence XAFS spectra of all PM (Table 1) were recorded at room temperature, respectively on beamlines 4–3 of the Stanford Synchrotron Radiation Laboratory (SSRL), California, and X-19A of the National Synchrotron Light Source (NSLS), New York. The beam was monochromatized using Si(220) or Si(111) double crystal monochromator. Harmonic rejection was achieved by detuning the incoming beam by 30% for Ni and 70% for S. All measurements were made using a Lytle or 13-element Ge array detector (*21*). Spectra of elemental Ni and S were recorded for calibration purposes either simultaneously with the sample or thereafter. XAFS spectra of numerous reference Ni and S compounds (sulfate, sulfide, oxides, nitrate, etc.) were also acquired. They were selected based on information obtained from various sources including toxicological studies and studies involving fossil fuels (*22*) and derivatives (*23*). The phase purity of reference compounds was verified by XRD, which showed no detectable impurity.

Analysis of EXAFS Data. All the scans were energy calibrated with respect to elemental S or Ni, then averaged to improve the signal-to-noise ratio. Standard procedures
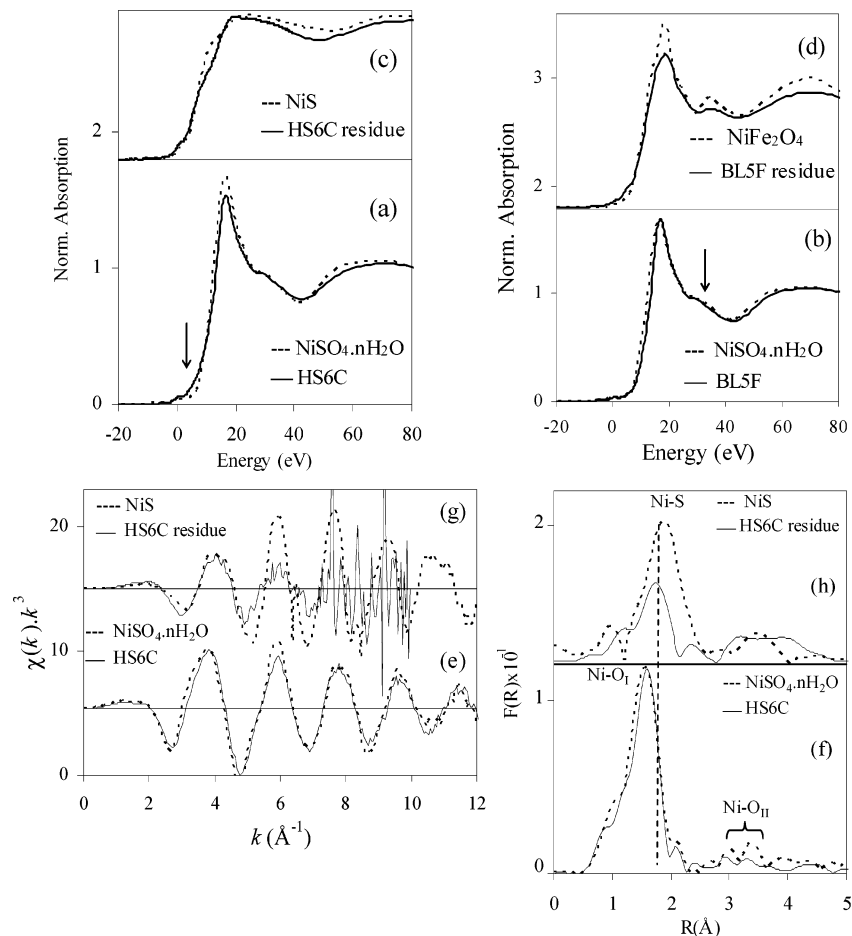
FIGURE 2. Ni K-edge XANES spectra of (a) HS6C, (b) BL5F, (c) HS6C residue, and (d) BL5F residue compared with reference compound spectra; EXAFS of (e) HS6C, and (g) its residue, and RSF of (f) HS6C, and (h) its residue compared with reference compound spectra.
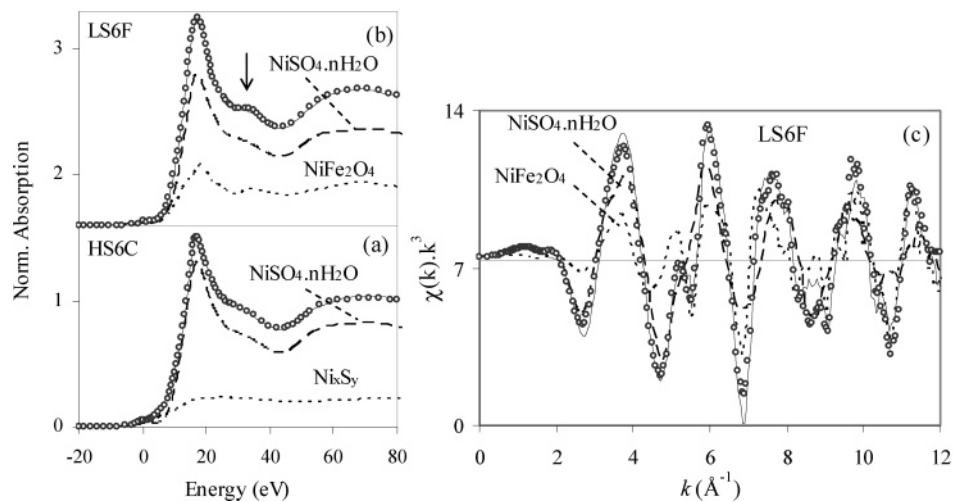

FIGURE 3. Ni speciation in the XANES region of (a) HS6C and (b) LS6F, and (c) in the EXAFS region of LS6F, and the observed (—), calculated (ooo), and the probable species derived from these fits (---).

were followed for background subtraction, normalization, and extraction of EXAFS functions $\chi(k)$ using WinXAS package (24). Fourier transform of k^3 weighted $\chi(k)$ function render radial structure function (RSF) where individual atom-pair interactions could be discerned at various distances. A parametrized theoretical curve of a well defined atomic cluster was then fitted to a few selected peaks in the RSF using a nonlinear least-squares fitting algorithm over a radial distance range as given elsewhere. Structural parameters determined in a fit include the number of atoms in a shell (N) about the absorbing atom, the distance (d) to that shell, and the mean-square displacement (σ^2) of the distance between the absorbing atom and the backscattering atoms for a single scattering path of photoelectron. The ab initio phase and amplitude parameters for theoretical modeling are derived from reference compounds employing FEFF7 code (25). The number of independent fit parameters (N_{indp}) was limited, by Nyquist theorem to $N_{indp} = (2\Delta k \Delta R / \pi) + 2$, where Δk and ΔR are, respectively the widths in k- and r-spaces used in the data analysis (26). The amplitude reduction

TABLE 2. Ni Speciation in PM Derived from Linear Combination XANES and EXAFS Fits

coarse PM$_{2.5+}$	Fe/Ni ratio[a]	Ni speciation (in %)		ΔE_0(eV)		R^d (%)
		NiSO$_4$·nH$_2$O	Ni$_x$S$_y$	NiSO$_4$·nH$_2$O	Ni$_x$S$_y$	
HS6C	1.0	82[b]	18	0.02	−0.09	1.5
BL5C	0.5	83	17	−0.14	−0.04	1.4
MS6C	1.2	85	15	0.17	−0.72	1.5
LS6C	1.6	78	22	0.17	0.03	2.0
fine PM$_{2.5}$		NiSO$_4$·nH$_2$O	NiFe$_2$O$_4$	NiSO$_4$·nH$_2$O	NiFe$_2$O$_4$	
HS6F	0.5	95 [96][c]	05 [04]	0.18	0.02	1.2
BL5F	0.4	92 [97]	08 [03]	−0.44	0.02	2.1
MS6F	0.6	95 [93]	05 [07]	0.15	0.01	1.1
LS6F	1.0	71 [75]	29 [25]	−0.19	0.03	1.3
BL6F	0.85	100	0	n/a	n/a	n/a

[a] Fe/Ni ratio calculated based on data given in Table 1. [b] Estimation of Ni species from linear combination XANES fits. [c] Estimation of Ni species from linear combination EXAFS fits. [d] R, residual factor (%).

TABLE 3. Ni Coordination in ROFA PM: Distance (d), Debye−Waller Factor (σ^2), Coordination Number (N) and Energy Shift (ΔE_0)

sample	shell	d/Å	σ^2/Å^2	N	ΔE_0/eV	R^a
HS6C	Ni−O	2.06	0.007	5.5	−1.4	9.8
BL5C	Ni−O	2.06	0.007	5.2	−1.2	9.6
MS6C	Ni−O	2.06	0.007	4.6	−1.2	11
LS6C	Ni−O	2.07	0.007	3.9	+0.1	12
BL6F	Ni−O	2.04	0.005	6	−4.7	10
HS6F	Ni−O	2.05	0.006	6	−4.3	7
BL5F	Ni−O	2.05	0.005	6	−3.6	6
MS6F	Ni−O	2.05	0.006	6	−4.5	5.8
LS6F	Ni−O	2.05	0.006	6	−3.3	7.3
	Ni−Fe/Ni[b]	2.94	0.007	2.5	−8.6	
	Ni−Fe	3.44	0.006	1.3	−5.8	
NiFe$_2$O$_4$	Ni−O	2.04	0.002	6	−10.9	14
	Ni−Fe/Ni[b]	2.96	0.008	12	−4.7	
	Ni−Fe	3.42	0.005	6	−17.5	
NiSO$_4$.nH$_2$O	Ni−O	2.05	0.007	6	−3.8	10
NiSO$_4$.7H$_2$O[29]	Ni−O	2.03		4		
		2.08		2		
NiS−trigonal[31]	Ni−S	2.31		5		
NiS-hexagonal[32]	Ni−S	2.39		6		

[a] R, residual factor (in %) [b] Co being used as second shell back-scatterer in place of Ni and Fe for least-squares refinement.

factor (S_o^2) was set at 0.9 for all the fits. An initial estimation of S_o^2 and ΔE_o was made by performing EXAFS fit on reference Ni compounds. Note, the zero-point of energy in the S and Ni K-edges XANES is in reference to 2472 eV for former and 8333 eV for latter.

Results and Discussion

XANES Studies. *Sulfur Speciation.* Figure 1a compares the S K-edge XANES spectra of two PM$_{2.5}$ samples obtained from same oil (HS6 oil) burned in *different combustors* (FTB and RLC). Whereas the spectra of both PM fractions obtained from *different oils* burned in same combustor (FTB) are compared in Figure 1b. Such comparisons are necessary to understand the effects of combustion conditions and fuel compositions on the final S-forms in size fractionated ROFA PM. Initially the different S-forms are identified through comparison of the PM spectra with those of analogous reference compounds. The comparison reveals that the PM$_{2.5}$ produced in RLC (i.e., BL6F) exhibits a lone sulfate peak (Figure 1a) while those produced in FTB are more complex, containing sulfate as the major S-form, and sulfide, thiophenic sulfur, and elemental sulfur as minor S-forms (Figure 1b).

To derive quantitative information, the S K-edge XANES spectra of all the FTB generated PM are deconvoluted into individual components by fitting a series of pseudo-voigt profiles to the main peaks (i.e., s→p transition) and arc-tangent step functions to edge jumps (i.e., transition of photoelectron to continuum) (Figure S1, Supporting Information). Using a standard calibration procedure the integrated areas under these peaks are transformed into percentages of the total sulfur contained by each identified S-form (27). They are presented schematically in Figure 1c and d respectively for PM$_{2.5+}$ and PM$_{2.5}$. The results show that regardless of the sulfur content of the oils, sulfate remains the predominant form of sulfur in all PM$_{2.5}$ (Figure 1d). This was followed by thiophenic sulfur. Increasing S content in the oils results in an increase in thiophenic sulfur and decrease in sulfate in both PM fractions (Figure 1c and d). Consequently, thiophenic sulfur becomes predominant in PM$_{2.5+}$ as the S content in oil reaches 1.6 wt. % (Figure 1c). A more recent S K- and L-edges XANES study of petroleum coke (a residuum fraction from refinery with typical S content 1−4 wt. %) also revealed thiophenic sulfur as the dominant form, while sulfate, inorganic sulfide (S$_2^{2-}$) and elemental sulfur were found in lesser amounts (23). Thiophenic sulfur is stable under lower combustion temperature. Thus thiophenic sulfur in the crude oil persists into end products such as coke and FTB generated PM. Thiophenic sulfur, inorganic sulfide, and sulfate were also found in a previous study of coal sulfur speciation (22). In most PM from FTB, elemental S appears to be the minor form. Sulfide formation is detected when the S content of oil exceeds 1.73 wt. %. In contrast, sulfate was the only S-form (Figure 1a) in the lone PM$_{2.5}$ (BL6F) from RLC (Table 1).

Nickel Speciation. Figure 2a and b show Ni K-edge XANES spectra of HS6C and BL5F. They are compared with that of NiSO$_4$.nH$_2$O. In general, the pre-edge peak (at ∼ 0 eV) appears because of a 1s→3d electronic transition. Since NiSO$_4$·nH$_2$O has Ni^{2+} ion in an almost centro-symmetric octahedral (O$_h$) site, this electric-dipole transition is forbidden by parity considerations. In such a case, electric quadrupole coupling is the most likely mechanism (28). The pre-edge and main-edge of both PM samples resemble that of NiSO$_4$·nH$_2$O. Consequently, much of the Ni in PM is divalent, coordinated octahedrally to oxygens. It is to be noted, however, that certain absorption features in both PM (as indicated by ↓ in Figure 2a for PM$_{2.5+}$ and Figure 2b for PM$_{2.5}$) cannot be explained by NiSO$_4$·nH$_2$O alone. Although these subtle features bear some attributes of a minor Ni form, the identity of the minor Ni form was not always evident in the XANES of an as-received PM. In fact EXAFS data corroborate this (Figure 2e and f). Conversely, the lack of such features in BL6F suggests that nickel exists exclusively as NiSO$_4$·nH$_2$O (Figure S2, Supporting Information).

Aqueous leaching of FTB PM shows dissociation of the major nickel sulfate into the leaching solution. The undissociated minor Ni species mainly remains in the insoluble residue. The identity of the minor Ni form became clear when
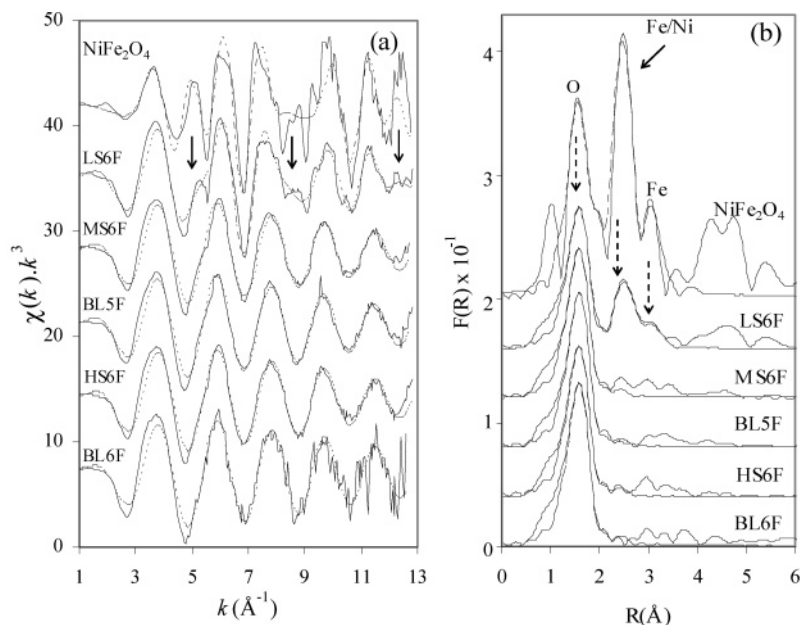
FIGURE 4. Ni K-edge observed (—) and calculated (---) (a) EXAFS and (b) RSF of all ROFA $PM_{2.5}$ samples and of $NiFe_2O_4$.

the aqueous residues spectra were compared with those of known references (Figure 2c and d). The comparisons reveal the minor Ni-form in $PM_{2.5}$ to be nickel ferrite, $NiFe_2O_4$ (Figure 2d), while that in $PM_{2.5+}$ is yet unknown (Figure 2c). Subsequent comparisons in EXAFS region preclude the presence of Ni_3S_2 and NiS_2 in HS6C residue (Figure S3). But HS6C residue does show some resemblance to NiS (Figure 2g). Their amplitudes differ markedly though, suggesting Ni is coordinated to fewer S in HS6C than six as in NiS. Moreover, a short Ni–S distance (Figure 2h) is not compatible with a coordination number of 6. This observation led us to conclude that the minor Ni form in $PM_{2.5+}$ is probably not NiS but a close relative, Ni_xS_y phase. Consequently, a linear combination of Ni K-edge XANES spectra of $NiSO_4 \cdot nH_2O$ and $NiFe_2O_4$, and $NiSO_4 \cdot nH_2O$ and Ni_xS_y (HS6C residue spectrum is used as proxy for Ni_xS_y) were fitted to those of the as-received LS6F and HS6C respectively, to estimate the amount of each Ni-form in different PM. Figures 3a and b show the typical Ni K-edge XANES fits along with the probable species derived from these fits for different PM fractions. Complementary information may be obtained by performing similar fits in the EXAFS region for all $PM_{2.5}$ samples (Figure 3c). The EXAFS fit for $PM_{2.5+}$ samples were not performed due to the lack of quality Ni_xS_y data (Figure 2g).

The results of the two fitting approaches compiled in Table 2, agree well, which includes the identified components, their amounts, and the residual factor for each fit. The results show regardless of the PM size, oil compositions, and combustion conditions, bio-available $NiSO_4 \cdot nH_2O$ appears to be the dominant nickel form. In agreement, the solubility study of metals indicates that 85–90% of Ni in PM is water soluble (19). The insoluble Ni resides as nickel ferrite ($NiFe_2O_4$) in all $PM_{2.5}$. The underlying mechanism for ferrite formation in PM can be hypothesized as follows: Often in fine particulates, metals (i.e., Fe and Ni) tend to settle on the surface of a PM (2) and are likely to oxidize. Under prevailing condition these oxides coprecipitate to form $NiFe_2O_4$. Note the increasing ferrite content in response to decreasing S content of the oil and increasing Fe/Ni ratio in the $PM_{2.5}$ samples (Table 2). Increased ferrite formation means more Ni becomes immobile and, therefore, less toxic.

Nickel EXAFS Studies. *$PM_{2.5+}$ Samples.* Figure 2e compares Ni K-edge EXAFS of a typical $PM_{2.5+}$ sample (HS6C) with that of $NiSO_4 \cdot nH_2O$. In $NiSO_4 \cdot nH_2O$ the Ni–O distances

lay in the range 2.031–2.078 Å, with each Ni surrounded by six water molecules (29). The water molecules, in turn, are hydrogen bonded to oxygen atoms of surrounding sulfate ions, resulting in a second $Ni-O_{II}$ shell. These two shells are present in the RSFs of both $NiSO_4 \cdot nH_2O$ and HS6C (Figure 2f). The RSFs are not corrected for the phase shift, so the peaks in the RSF appear at shorter distances than the true near-neighbor distances. The EXAFS analysis of the second $Ni-O_{II}$ shell, in particular, is difficult as it is obscured by the multiple scattering (MS) from the first $Ni-O_I$ shell (30). Nonetheless, the similarities between the PM and $NiSO_4 \cdot nH_2O$ data (Figure 2e and f) suggest the latter being the major constituent of the PM.

In addition, the XANES data show the presence of a minor Ni_xS_y phase in all $PM_{2.5+}$. As shown earlier, the Ni–S distance in Ni_xS_y is longer (31, 32) than the Ni–O distance in $NiSO_4.nH_2O$ (Figure 2h and Table 3). Thus if the PM were to have significant Ni_xS_y, either a split or a broadening in the first RSF peak is inevitable, in which case the EXAFS data having resolution ΔR ($=\pi/2\Delta k$) of 0.16 Å, can identify the presence of nickel sulfide by differentiating between first shell Ni–O and Ni–S bonds. In contrast the first RSF peak of HS6C (Figure 2f) shows no appreciable broadening or split, implying that the Ni–S contribution to RSF is rather trivial. In agreement, the EXAFS data of all $PM_{2.5+}$ samples are in phase with that of $NiSO_4 \cdot nH_2O$ over the entire k range (Figure 2e). This match in frequency indicates that the first shell Ni–O distances in all PM are nearly identical to that of $NiSO_4 \cdot nH_2O$, and that nickel in PM is mostly coordinated by water molecules as in nickel sulfate.

In order to obtain the Ni–O bond parameters, the fitting to the backtransformed Ni–O EXAFS was performed in k space, in the range $2.0 - 12 \text{ Å}^{-1}$. To avoid correlation between σ^2 and N, the former was fixed at 0.007 $Å^2$ based on fit to $NiSO_4 \cdot nH_2O$, and the latter was allowed to float. This way, a more precise and consistent N value may be obtained for all $PM_{2.5+}$ samples. The fit appears satisfactory for all PM (Figure S4). The best-fit Ni–O bond parameters for all samples are summarized in Table 3. The results give Ni–O distances and coordination numbers in the ranges 2.06–2.07 Å and 5.5–3.9 respectively. An increasing Ni–O distance with decreasing coordination number seems unrealistic, however (Table 3). On the other hand, fitting the filter EXAFS with a fixed coordination number (i.e., $N = 6$) and variable σ^2 did

not give any satisfactory fit (Figure S5 and Table S1, Supporting Information). A gradual drop in the first RSF peak height and a small upward shift of Ni−O peak with decreased S content in the oils (Figure S6, Supporting Information) is compatible with decreased sulfate and increased sulfide (Table 2). An anticipated result of such changes would be an increase in Ni−O distance and decrease in coordination number, in agreement with the results obtained from EXAFS fits (Table 3). That is to say a decreased S content of oil favors nickel sulfide formation, in contrast to XANES result of increased S favoring increase in all sulfides including nickel sulfide. Last, for all samples the large σ^2 value arises from fitting EXAFS data with a single Ni−O distance, rather than multiple distances which represent the true Ni−O environment.

PM_2.5 Samples. Figure 4a and b (solid line) show the Ni K-edge EXAFS and RSF of all PM$_{2.5}$ samples (Table 1) and of NiFe$_2$O$_4$. Most PM spectra resemble NiSO$_4$·nH$_2$O, much like their PM$_{2.5+}$ counterparts. In addition, LS6F exhibits some spectral features that are characteristic of NiFe$_2$O$_4$ (see ↓ in Figure 4a). These features are not so evident in other spectra suggesting lower NiFe$_2$O$_4$ contents in the remaining PM$_{2.5}$ samples. Given the level of NiFe$_2$O$_4$ in LS6F (Table 2), the Ni−O peak of NiFe$_2$O$_4$ would superimpose on that of NiSO$_4$·nH$_2$O. Fortunately, in NiFe$_2$O$_4$, Ni has 6O neighbors with an average Ni−O distance of 2.04 Å (*33*), similar to the corresponding bond parameters in NiSO$_4$·nH$_2$O. This similarity in the Ni−O environments allows an unambiguous determination of Ni−O bond parameters for all PM from EXAFS.

At a further distance, Ni in NiFe$_2$O$_4$ has (6Ni + 6Fe) atoms in the second shell at 2.954 Å and 6Fe atoms in the third shell at 3.457 Å (*33*). Thus the two peaks just outside the Ni−O peak in the RSF, are attributed to the above two shells (Figure 4b). Despite the difference in their individual peak heights, these two peaks of LS6F appear at about the same distances as those of NiFe$_2$O$_4$. Based on this analogy, the second peak at ~2.5 Å was assigned to Ni−(Ni/Fe) shell and the third at ~3.0 Å to Ni−Fe shell in the RSF of LS6F (Figure 4b). Comparison of the back-transformed Ni−(Ni/Fe) peaks of LS6F and NiFe$_2$O$_4$ shows that they are in phase, with the former exhibiting roughly one third the amplitude of latter (Figure S7, Supporting Information), giving a clue to the number and types of second shell backscatters about Ni in LS6F.

Meaningful structural parameters for the first three shells (i.e., Ni−O, Ni−(Ni/Fe), and Ni−Fe) are obtained using ab initio phase and amplitude parameters of all paths based on NiFe$_2$O$_4$ model, with the exception of Ni−(Ni/Fe) path. Because the second shell Fe/Ni backscatterers (with $Z = 26$ and 28) exhibit similar amplitudes and phase shifts they cannot be easily differentiated from each other as second-shell backscatterers by EXAFS. Moreover, fitting the second shell with all Ni or all Fe backscatters would probably yield a less precise N value. On the other hand, by substituting both Ni and Fe with an intermediate Co atom (Figure S8, Supporting Information) a more realistic N value may be obtained. Thus, the Ni coordination in NiFe$_2$O$_4$ was modeled by placing six O in the first shell, 12 Co in the second shell, and six Fe in the third shell. The MS contribution from the first Ni−O$_6$ shell was ignored as it contributes little to the radial distance range investigated. The refinement was performed in the *r*- space over a radial distance range $\Delta R = 0.95−2.1$ Å for Ni−O peak alone, or 0.95 − 3.28 Å when all three peaks are included. The fits to the observed data are satisfactory (Figure 4a and b). The results listed in Table 3 show that the first shell Ni−O$_6$ distances lay in the range 2.04−2.05 Å close to that in NiSO$_4$·nH$_2$O. No significant differences in the fitted Ni−O distances were observed between individual samples, indicating NiSO$_4$·nH$_2$O as the

major Ni species in all PM$_{2.5}$ samples. The Ni−Ni/Fe and Ni−Fe distances of LS6F (at ca. 2.94 Å and 3.44 Å) are close to those of bulk NiFe$_2$O$_4$. The best fit for LS6F was obtained with roughly 2.5 Co atoms in the second shell around Ni. This amounts to LS6F comprising 21% NiFe$_2$O$_4$ and 79% NiSO$_4$·nH$_2$O, in agreement (within experimental error) with those obtained from the linear combination EXAFS and XANES fits (Table 2). An absence of characteristic Ni−Ni/Fe or Ni−Fe peaks precludes the presence of NiFe$_2$O$_4$ in the lone PM$_{2.5}$ from RLC (BL6F). The finding that the Ni in PM$_{2.5}$ produced in RLC is more bioavailable than that produced in FTB is significant as the former can be potentially more toxic. The reduction in toxicity of the latter is caused by part of the Ni being immobilized due to the formation of insoluble nickel ferrite.

Acknowledgments

Supporting Information Available

XAFS figures and a table. This material is available free of charge via the Internet at http://pubs.acs.org.

Literature Cited

(1) Dockery, D. W.; Pope, C. A. Out Side Air 1: Particulates. In *Topics in Environmental Epidemiology*; Steenland, K.; Savitz, D. A. Eds.; Oxford University Press: New York, 1997; pp 119−166.

(2) Nel, A. Air pollution-related illness: Effects of particles. *Science* **2005**, *308*, 804−806, and references therein.

(3) Bachmann, J. D.; Damberg, R. J.; Caldwell, J. C.; Edwards, C.; Koman, P. D. *Review of the National Ambient Air Quality Standards for Particulate Matter: Policy Assessment of Scientific and Technical Information*, (OAQPS Staff Paper), EPA-452/R-96−031 (NTIS PB97−11540.6); U.S. Environmental Protection Agency: Washington, DC, 1996.

(4) Wolff G. T. *Closure by the Clean Air Science Advisory Committee (CASAC) on the staff paper for particulate matter,* EPA-SAB-CASAC-LTR-96−008. June 13, 1996; U. S. Environmental Protection Agency, Washington, DC, 1996.

(5) Dreher, K. L.; Jaskot, R.; Richards, J. H.; Lehmann, J. R.; Winsett, D.; Hoffman, A.; Costa D. L. Acute pulmonary toxicity of size-fractionated ambient air particulate matter. *Am. J. Respir. Crit. Care. Med.* **1996**, *153*, A15.

(6) Dheher, K. L.; Jaskot, R. H.; Lehmann, J. R.; Richards, J. H.; McGee, J. K.; Ghio, A. J.; Costa, D. L. Soluble transition metals mediated residual oil fly ash induced lung injury. *J. Toxicol. Environ. Health* **1997**, *50*, 285−305.

(7) Goldsmith, C. A.; Imrich, A.; Danaee, H.; Ning, Y. Y.; Kobzik, L. Analysis of air pollution particulate-mediated oxidant stress in alveolar macrophages. *J. Toxicol. Environ. Health* **1998**, *54*, 529−545.

(8) Knaapen, A. M.; Shi, T.; Borm, P. J.; Schins, R. P. Soluble metal as well as the insoluble particle fractions are involved in cellular DNA damage induced by particulate matter. *Mol. Cell Biochem.* **2002**, *234/235*, 317−326.

(9) Prahalad, A. K.; Inmon, J.; Dailey, L. A.; Madden, M. C.; Ghio, A. J.; Gallagher, J. E. Air pollution particles mediated oxidative DNA damage in a cell free system and in human airway epithelial cells in relation to particulate metal content and bioreactivity. *Chem. Res. Toxicol.* **2001**, *14*, 879−887 and references therein.

(10) Bhatnagar, A. Cardiovascular Pathophysiology of Environmental Pollutants. *Am. J. Physiol. Heart Circ. Physiol.* **2004**, *286*, H479−H485.

(11) Salnikow, K.; Li, X.; Lippmann, M. Effect of nickel and iron co-exposure on human lung cells. *Toxicol. Appl. Pharmacol.* **2004**, *196*, 258 − 265 and references therein.

(12) Prieditis, H.; Adamson, I. Y. Comparative pulmonary toxicity of various soluble metals found in urban pollution dusts. *Exp. Lung Res.* **2002**, *28*, 563−576.

(13) Wilson, M. R.; Lightbody, J. H.; Donaldson, K.; Sales, J.; Stone, V. Interactions between ultrafine particles and transition metals in vivo and in vitro. *Toxicol. Appl. Pharmacol.* **2002**, *184*, 172−179.

(14) *EPA Open House Highlight Research on Harmful Effect of Airborne Particles,* http://www.epa.gov/nheerl/ordpr/1998/pr101398.pdf, (accessed October 13, 1998).

(15) Kodavanti, U. P.; Schladweiler, C. M.; Ledbetter, A. D.; Hauser, R.; Christiani, D. C.; Samet, J. M.; McGee, J.; Richards, J. R.; Costa, D. L. Pulmonary and systemic effects of zinc-containing emission particles in three rat strains: Multiple exposure scenarios. *Toxicol. Sci.* **2002**, *70*, 73−85.

(16) Gaillard, J. F.; Webb, S. M.; Quintana, J. P. G. Quick X-ray absorption spectroscopy for determining metal speciation in environmental samples. *J. Synchrotron Radiat.* **2001**, *8*, 928−930 and references therein.

(17) Ressler, T.; Wong, J.; Roos, J.; Smith, I. L. Quantitative speciation of Mn-bearing particulates emitted from autos burning (methylcyclopentadienyl)manganese tricarbonyl-added gasolines using XANES spectroscopy. *Environ. Sci. Technol.* **2000**, *34*, 950−958.

(18) Pattanaik, S.; Huggins, F. E.; Huffman, G. P.; Linak, W. P.; Miller, C. A. XAFS Spectroscopy Analysis of the molecular structure of metal and sulfur in fine particulate matter (PM) derived from the combustion of residual oil. Presented at the 222nd ACS National Meeting, August 2001; Vol. 46, 626−628.

(19) Linak, W. P.; Miller, C. A.; Wendt, J. O. L. Comparison of particle size distributions and elemental partitioning from the combustion of pulverized coal and residual fuel oil. *J. Air Waste Manage. Assoc.* **2000**, *50,* 1532−1544 and references therein.

(20) Linak, W. P.; Miller, C. A.; Wendt, J. O. L. Fine particle emissions from residual fuel oil combustion: Characterization and mechanisms of formation. *Proc. Comb. Inst.* **2000**, *28*, 2651−2658.

(21) Cramer, S. P.; Tench, O.; Yocum, M.; George, G. N. A 13-element Ge detector for fluorescence EXAFS. *Nucl. Instrum. Metheds, A* **1988**, *266*, 586−591.

(22) Kasrai, M.; Brown, J. R.; Bancroft, G. M.; Yin, Z.; Tan, K. H. Sulfur characterization in coal from X-ray absorption near-edge spectroscopy. *Int. J. Coal Geol.* **1996**, *32*, 107 - 135.

(23) Hay, S. J.; Metson, J. B.; Hyland, M. M. Sulfur speciation in aluminum smelting anodes. *Ind. Eng. Chem. Res.* **2004**, *43*, 1690−1700.

(24) Ressler, T. WinXAS: A Program for X-ray absorption spectroscopy data analysis under MS-Windows. *J. Synchrotron Radiat.* **1998**, *5*, 118−122.

(25) Zabinsky, S. I.; Rehr, J. J.; Aukudinov, A. FEFF Code for *ab initio* Calculation of XAFS. Ph.D. Thesis, University of Washington, **1996**.

(26) Stern, E. A. Number of relevant independent points in X-ray-absorption fine-structure spectra *Phys. Rev. B* **1993**, *48*, 9825−9827.

(27) Huffman, G. P.; Huggins, F. E.; Shah, N.; Huggins, R.; Linak, W. P.; Miller, C. A.; Pugmire, R. J.; Meuzelaar, H. L. C.; Seehra, M. S.; Manivannan, A. Characterization of fine particulate matter produced by combustion of residual fuel oil. *J. Air Waste Manag. Assoc.* **2000**, *50*, 1106−1114 and references therein.

(28) Shulman, G. R.; Yafet, Y.; Eisenberger, P.; Blumberg, W. E. Observations and interpretation of X-ray absorption edges in iron compounds and proteins. *Proc. Natl. Acad. Sci. U.S.A.* **1976**, *73*, 1384−1388.

(29) Ptasiewicz-Bak, H.; Olovsson, I.; McIntyre, G. J. Charge density in orthorhombic $NiSO_4 \cdot 7H_2O$ at room temperature and 25K. *Acta Cryst., B* **1997**, *53*, 325−326.

(30) Lindqvist-Reis, P.; Muñoz-Páez, A.; Diaz-Moreno, S.; Pattanaik, S.; Persson, I.; Sandström, S. The structure of the hydrated gallium(III), indium(III), and chromium(III) ions in aqueous solution. A large angle X-ray scattering and EXAFS study. *Inorg. Chem.* **1998**, *37*, 6675−6683.

(31) Rajamani, V.; Prewitt, C. T. The crystal structure of millerite *Can. Mineral.* **1974**, *12*, 253−257.

(32) Trahan J.; Goodrich R. G.; Watkins S. F. X-ray diffraction measurements on metallic and semi- conducting hexagonal NiS. *Phys. Rev Series 3B Solid State 2,* **1970**, 2859−2862.

(33) Subramanyam, K. N. Neutron and X-ray Diffraction studies of certain doped nickel ferrites. *J. Phys. C* **1971**, *4*, 2266−2268.